International Journal of Mechanical, Industrial and Aerospace Sciences
ISSN: 2517-9950
Vol:13, No:11, 2019

Numerical and Experimental Comparison of Surface Pressures around a Scaled Ship Wind-Assisted Propulsion System

James Cairns, Marco Vezza, Richard Green, Donald MacVicar

Abstract**—**Significant legislative changes are set to revolutionise the commercial shipping industry. Upcoming emissions restrictions will force operators to look at technologies that can improve the efficiency of their vessels -reducing fuel consumption and emissions. A device which may help in this challenge is the Ship Wind-Assisted Propulsion system (SWAP), an actively controlled aerofoil mounted vertically on the deck of a ship. The device functions in a similar manner to a sail on a yacht, whereby the aerodynamic forces generated by the sail reach an equilibrium with the hydrodynamic forces on the hull and a forward velocity results. Numerical and experimental testing of the SWAP device is presented in this study. Circulation control takes the form of a co-flow jet aerofoil, utilising both blowing from the leading edge and suction from the trailing edge. A jet at the leading edge uses the Coanda effect to energise the boundary layer in order to delay flow separation and create high lift with low drag. The SWAP concept has been originated by the research and development team at SMAR Azure Ltd. The device will be retrofitted to existing ships so that a component of the aerodynamic forces acts forward and partially reduces the reliance on existing propulsion systems. Wind tunnel tests have been carried out at the de Havilland wind tunnel at the University of Glasgow on a 1:20 scale model of this system. The tests aim to understand the airflow characteristics around the aerofoil and investigate the approximate lift and drag coefficients that an early iteration of the SWAP device may produce. The data exhibits clear trends of increasing lift as injection momentum increases, with critical flow attachment points being identified at specific combinations of jet momentum coefficient, Cμ, and angle of attack, AOA. Various combinations of flow conditions were tested, with the jet momentum coefficient ranging from 0 to 0.7 and the AOA ranging from 0° to 35°. The Reynolds number across the tested conditions ranged from 80,000 to 240,000. Comparisons between 2D computational fluid dynamics (CFD) simulations and the experimental data are presented for multiple Reynolds-Averaged Navier-Stokes (RANS) turbulence models in the form of normalised surface pressure comparisons. These show good agreement for most of the tested cases. However, certain simulation conditions exhibited a well-documented shortcoming of RANS-based turbulence models for circulation control flows and over-predicted surface pressures and lift coefficient for fully attached flow cases. Work must be continued in finding an all-encompassing modelling approach which predicts surface pressures well for all combinations of jet injection momentum and AOA.

Keywords**—**CFD, circulation control, Coanda, wing sail, wind tunnel.

J. Cairns, PhD researcher, is with the Aerospace Sciences Research Division, James Watt Building, University of Glasgow, Glasgow, G12 8QQ, UK (phone: +44 744 752 0293; e-mail: j.cairns.1@research.gla.ac.uk).

M. Vezza, a senior lecturer is with the Aerospace Sciences Research Division, James Watt Building, University of Glasgow, Glasgow, G12 8QQ, UK (phone: +44 141 330 4107; e-mail: marco.vezza@glasgow.ac.uk).

R. Green, a senior lecturer is with the Aerospace Sciences Research Division, James Watt Building, University of Glasgow, Glasgow, G12 8QQ, UK (phone: +44 141 330 4312; e-mail: Richard.green@glasgow.ac.uk).

D. MacVicar is with the CTO at SMAR Azure LTD, 14-18 Hill Street, Edinburgh, EH2 3JZ, UK (phone: +44 131 610 7627; e-mail: donald@smar-azure.com).

I. Introduction

ENERGY use and the environment are among the key issues facing society in the coming years. The UN lists both climate change and, more specifically, marine shipping and pollution as some of the main global issues in need of immediate worldwide action [1].

As a result, major legislation changes are set to be introduced and perhaps instigate a movement away from traditional fossil fuel based propulsion systems and towards cleaner alternatives. The International Maritime Organization (IMO) are tightening restrictions on sulphur dioxide emissions by stipulating that fuels must have a maximum sulphur content of no more than 0.5 m/m (mass by mass) by 2020 [2]. This change is just one aspect of a wider IMO ambition to reduce shipping related greenhouse gas emissions by 70%, relative to the level in 2008 [3], which will certainly mean further restrictive legislation is immanent.

The scale of this challenge cannot be understated and a large requirement is placed on the finding of alternative propulsion systems to reach targets. Lloyd's Register's Low Carbon pathways report identified that, for most of the decarbonisation measures they investigated, "a substitute for fossil fuel [is required], because energy efficiency improvements alone will not be sufficient [to reach these goals] in the medium to longer term" [4].

Fig. 1 Buckau - The first Flettner rotor ship [17]

The benefits of alternative energy sources extend to that of purely legislative and environmental issues and, as with

anything that is to be successfully integrated into a highly competitive market, also represent significant economic savings. Clearly, a reduction in fuel consumption is met with a reduction in fuel costs, but after considering the trade-offs between increased ship mass, reduction in payload capacity, large installation and retrofitting costs, multiple studies have found bottom line cost savings of between 5% and 10% per shipping route to be likely [5], [6].

II. Wind Ship Propulsion

For thousands of years humans have harvested wind power, be it from primitive sailboats dated to the 5th millennium BC [7], or by the vast wind turbine farms of today. Even still, there exists a huge amount of untapped, clean power available from the wind, especially over the large, flat and obstacle free ocean environment.

The so-called 'Age of Sail', roughly dated from the 15th through to the mid-19th centuries, was the heyday of wind ship propulsion [8]. During this time the sailing ship was king, superseding the oar propelled ships of previous times and instigating the Age of Discovery, allowing extensive overseas exploration and trade [9].

Although a classic, tall ship today conjures a beautiful image, riding the waves, sails billowing in the wind, the reality was that they were brutal and dangerous environments. Navigation of coastal and open waters, with complete reliance on favourable wind conditions, and no means of on demand propulsion left ships at mercy of the unrelenting wrath of the sea. The invention of the steam engine changed this reality forever, with steam powered propellers quickly replacing sails and ending the dominance of wind power.

Much more recently, research into wind assisted ship propulsion was reincarnated in the 1980s, catalysed by rapidly increasing oil prices as a result of an uncertain political and social climate. The 1973 oil crisis dramatically changed the existing shipping trends and initiated several government funded campaigns looking to find an alternative and feasible source of propulsion [10].

Within months oil prices returned to levels in line with the trends of the time which was reflected by an abandonment in developments of wind technology [11]. Since 1998, oil prices have been increasing at a rate more rapidly than even that of the crises of the 1970s, and this combined with the immanent legislative emissions restrictions, is reinstating wind power as an attractive commercial proposition.

A. Flettner Rotor

Flettner rotors are rotating cylinders which use the Magnus Effect to produce a propulsive force from the wind [12]. The Magnus effect is closely linked to the Bernoulli principle; the rotation causes higher wind speed on the side which the cylinder is rotating towards, and lower wind speed on the opposite side. This results in a pressure differential and thus a lifting force develops [13].

There is significant research on the lift and drag forces of rotating cylinders in a flow. Aoki and Ito [14] described the lift and drag characteristics as well as Strouhal number and flow patterns for rotating cylinders at different spin rates and Reynolds numbers. Their results show increasing lift and drag coefficient with increasing spin rate, however also they found unexplained discrepancies between their numerical model and experiment.

Thom [15] and Prantl [16] had previously reported similar results, finding that the lift of a cylinder was a function of the rotation rate although the exact correlation was not defined. The German physicist Anton Flettner was the first to physically apply the concept to propulsion of ships. His 1926 crossing of the Atlantic on a craft powered solely by twin rotating cylinders cemented the concept as a viable propulsive option [17]. This vessel, Buckau, is shown in Fig. 1.

Rapid development of diesel engines stalled further use of the Flettner rotor until it found reapplication in the carbon conscious environment of today. Currently there are multiple operating Flettner rotor ships with many more in early development. Norsepower offered the first commercially available retrofitting service. They deployed the Norsepower rotor sail on the Bore Ltd. owned M/S Estraden and reported fuel savings of 8% compared to the non-rotor configuration [18].

B. Kite

Having been initially viewed with some scepticism, the idea of using a towing kite is gaining some traction and several industrial parties are beginning to introduce designs [19], [20]. Differing from traditional sails in that they are attached to control lines rather than masts, kite rigs have many similarities with the kites used in wind sailing. Their double walled profile exhibits an aircraft-like wing shape in order to achieve high lift at low drag [21].

Naaijen and Koster [22] investigated the performance of kites as auxiliary propulsion for merchant ships. They concluded that, for the 50000 d.w.t. (dry weight tonnage) tanker investigated, fuel savings of up to 50% could be achieved by using a 500 m^2 kite attached to a 350 m towing line. Their study also investigated optimal towing altitudes to be approximately 30% of this line length and found that attachment to the bow of the ship minimised the required rudder angles and therefore offered minimal additional resistance.

Kukner et al. [21] investigated wind-based propulsion for small craft and highlighted some further benefits of the towing kite approach. A kite system working at 150-200 m above sea level is free from the turbulent boundary layer of wind and as a result has 30-70% more available energy compared to conventional sails. The force generated by the kite can be manipulated by the control lines so that the towing forces act close to the centre of gravity, eliminating any dangerous overturning moments that are inherent to cylindrical masts or sails.

Traut et al. [23] numerically compared the power contributions of Flettner rotors and a kite across five shipping routes. They found that the kite exhibited higher power volatility than the Flettner rotor, over both time and geographic location, and produced less averaged propulsive

force than two or more Flettner rotors. Despite this, advantages were noted for the kite in that it represents a truly zero carbon technology and takes up very little space on the deck. It was concluded that both wind propulsion methods where insufficient to fully power the craft and more conventional methods were required in tandem with either technology.

C. Actively Controlled Wing Sail

Actively controlled wing sails are vertically mounted wing shape sections which use boundary layer control to improve lift over a wide AOA range. The appearance is very similar to that of a Flettner rotor; a vertical mast albeit with a very thick aerofoil section rather than perfect cylinder. Contrary to Flettner rotors, the active wing sail utilises blowing and/or suction to energise the boundary layer and the only movement of the physical system is to orient the aerofoil favourably with respect to the wind [24].

The first ship to utilise actively controlled wing sail technology was the Moulin à Vent [25], as shown in Fig. 2. This experimental ship was funded by the Cousteau foundation and confirmed previous wind tunnel tests on smaller scale models. Having demonstrated the feasibility of such a craft, development was started on a larger active wing sail propelled ship, the 30 metre Alcyone. This ship differed slightly from the Moulin à Vent in that it featured two aerofoils of reduced aspect ratio rather than one. This was to reduce storm wind loading which had eventually led to failure of the preceding ship.

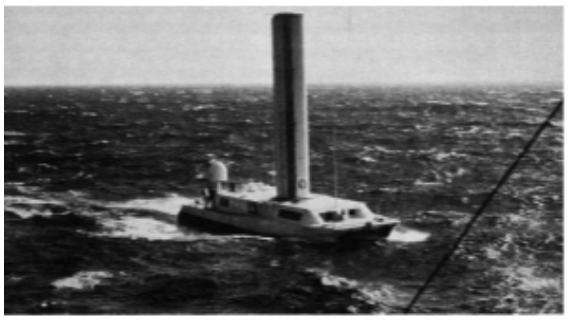

Fig. 2 The Moulin à Vent [26]

With regard to modern wind propulsion literature, actively controlled wing sails represent a comparatively sparse area. Hcini et al. [26] published a numerical method of predicting their aerodynamic performance. They confirmed their method with experiment and deemed their use of a vortex model as providing satisfactory representation of the performance characteristics of the active wing sail system. They concluded that the actively controlled wing sail offers a promising wind propulsion alternative but more experimental and theoretical results are required to prove its success.

Guerri et al. [27] performed numerical simulation of turbulent flow around an oval cross-section, active wing sail. Their geometry bears some resemblance to the SWAP iteration tested in this work - however only employing suction rather than a blowing/suction combination. Their results show the suction increases lift to drag ratio and suppresses vortex shedding, eliminating vortex induced vibration.

To the knowledge of the authors, no studies perform a detailed comparison of actively controlled wing sails with their biggest competitor, the Flettner rotor.

III. Circulation Control

The Coanda effect was first investigated for aerodynamic use by Henri Marie Coanda in 1935 and predominantly relates to the ways in which jet flows attach, entrain and mix with surrounding fluids in the presence of external walls [28]. The effect can be considered to encompass three main flow phenomena [29]. Firstly, a jet tangential to a curved surface tends to remain attached to that surface rather than continue in its original direction. Secondly, a free jet has the ability to attach itself to a close wall. Thirdly, jets flowing over curved surfaces by the Coanda effect tend to entrain more surrounding ambient fluid then that of straight wall enclosed jets, with some studies reporting up to 20 times increased entrainment by air volume [30]. These three processes are covered by the same underlying physical action; the presence of external walls acts to reduce the pressure on the wall side of the fluid due to viscous drag interaction between the fluid and the wall. This lower pressure creates an unbalanced force acting to deflect the fluid in the direction of the contacting wall [30].

Newman [31] proposed a relationship for the separation angle of Coanda flows stating that separation angle varies as a function of slot width, radius of curvature, pressure differential and fluid density and viscosity. His experimental study into two-dimensional separation of tangential jets from circular walls derived an empirical relationship for separation angle based upon these parameters.

The effect of Reynolds number on the reattachment points of Coanda jets is a point of particular interest when aerodynamic tests are required to be performed on small scale models. Past research in this area is limited, however Allery et al. [32] experimentally investigated the effect of Reynolds number (Re) on the attachment of a jet to a wall with inclination. They reported that for a constant inclination there is a critical Reynolds number at which the flow attaches Re_{ca} when increasing the jet velocity and a Reynolds number at which the flow detaches Re_{cd} when decreasing the jet velocity. For $Re_{cd} \leq Re \leq Re_{ca}$, the system was stable and only a large perturbation would cause attachment or detachment.

Recently, the progression of CFD technology and computing power has led to a renaissance in interest into circulation control applications with several experimental systems looking to improve aerodynamic efficiency across an ever-increasing range of cases [33].

Numerical simulation and prediction of circulating flows is a particularly difficult problem. RANS simulation have well documented issues when dealing with flows exhibiting strong streamline curvature; many of the more computationally

inexpensive models neglect anisotropic turbulence and numerous studies have shown that the linear stress-strain correlations used by standard Eddy Viscosity Models (EVMs) result in incorrect prediction of both lift and drag [34]. Rumsey and Nishino [35] compared RANS and LES (large-eddy simulation) approaches for the application of circulation control aerofoils, noting that models which do not account for streamline curvature tend to predict Coanda separation too late and even lead to non-physical solutions for high jet mass flows. They found that all RANS approaches predicted higher lift by approximately 15% compared to LES. The reasons for this tendency were not investigated but it was shown that it was not merely due to incorrect prediction of the jet separation point. Of the RANS models tested, the Spalart-Allmaras with curvature correction (SARC) model exhibited the smallest variation from LES.

In regard to RANS models, these findings have been confirmed by Swanson et al. [36] who found, compared to the SARC model, the SST and standard Spalart-Allmaras (SA) produce significantly greater delay in separation for Coanda jet applications. In later work, Swanson proposed a modification to the standard curvature correction parameters of the SA model, using the Cr_3 number as a tuning parameter for circulation control aerofoils [37]. It was proposed that the tendency for RANS models to over predict lift was due to too much high momentum fluid being transferred to the inner shear layer. By increasing the Cr_3 parameter, the production of turbulent kinetic energy was reduced and the separation occurred earlier along the upper surface. Although giving good results for the specific case studied, this method lacks validation over a general set of cases.

Zha and Paxton [38] proposed a now highly investigated method of circulation control, the co-flow jet (CFJ). Their numerical investigations showed dramatically increased lift, stall margin and drag reduction using both injection and suction with zero mass flux. An aperture near the leading edge (LE) injects air recycled from a suction slot near the trailing edge (TE). The strong turbulent diffusion and mixing from the jet enhances transport of energy from the jet flow to the free stream and allows the outer flow to overcome severe adverse pressure gradient, staying attached up to high angles of attack [39].

Fig. 3 illustrates one example of a CJF type aerofoil, the NREL S809 CFJ proposed by Xu et al. [40].

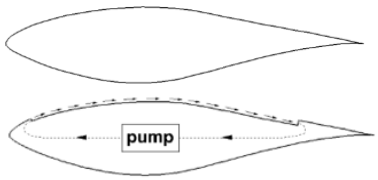

Fig. 3 NREL S809 baseline and NREL S809 CFJ cross-section [40]

A. Wind Tunnel

The experiments were conducted in the de Havilland wind tunnel at the University of Glasgow, which is part of the UK wide National Wind Tunnel Facility (NWTF). This is a low speed, closed-section facility with an octagonal test section of 2.65 m width, 2.06 m height and 5.60 m length. The inclusion of the octagonal corner fillets creates a slight increase in the area of cross section from inlet to outlet, compensating for boundary layer growth and offsetting resulting longitudinal static pressure gradients [41].

IV. Experimental Setup

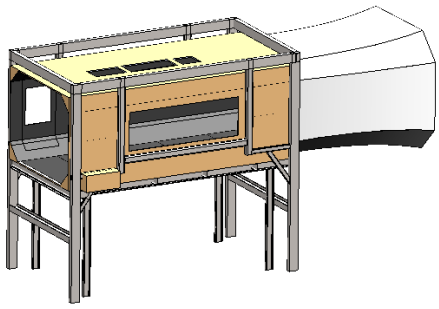

Fig. 4 de Havilland wind tunnel octagonal test section

The test section is vented to the atmosphere by a gap of around 0.05 m on the wall at the downstream edge. The fan has a diameter of 3 m and is located on the opposite side of the loop relative to the test section. The tunnel has a 5:1 contraction ratio and the turbulence level in the velocity range adopted in the present study (2m/s to 20m/s) is measured to be less than 1%.

Free stream temperature measurement is taken through a platinum resistance PT100 sensor mounted near the start of the test chamber. Additional temperature measurements were provided by a TOPELEK portable thermometer which allowed for measurement of the jet injection air temperature at the point where it exits the model in the working section.

The arrangement of the wind tunnel working section and model is shown in Fig. 5. This shows the notional arrangement of the model with other fittings and measurement probe positions.

The aerofoil itself was mounted on the wind tunnel turntable system and spanned from floor to roof. The turntable rotates about the vertical axis, thus setting the model AOA. The system used is an Ate AEROTECH 2 m diameter turntable which provides 360° motion at 5° s^{-1} with a position accuracy of ±0.005°.

Wind tunnel data acquired included the static pressures from the ceiling ahead of the test model, the Pitot-static pressure (dynamic pressure) for wind tunnel speed measurement, and also the contraction ring pressures for an additional dynamic pressure measurement. The aerofoil was fitted with surface pressure tappings which were connected to a ZOC22b and a ZOC23b pressure scanner by long, polythene tubes. The 3rZOC22b scanner has a ±2491 Pa range across 32 channels and the ZOC23b has a ±6895 Pa range across an additional 32 channels. For each data sample, 2 s of physical time was averaged using a sample period of $312.5x10^{-6}s$ across 64 channels over 100 individual data points. The data from the wind tunnel static, Pitot-static and contraction ring

ports were also recorded to the ZOC pressure scanners.

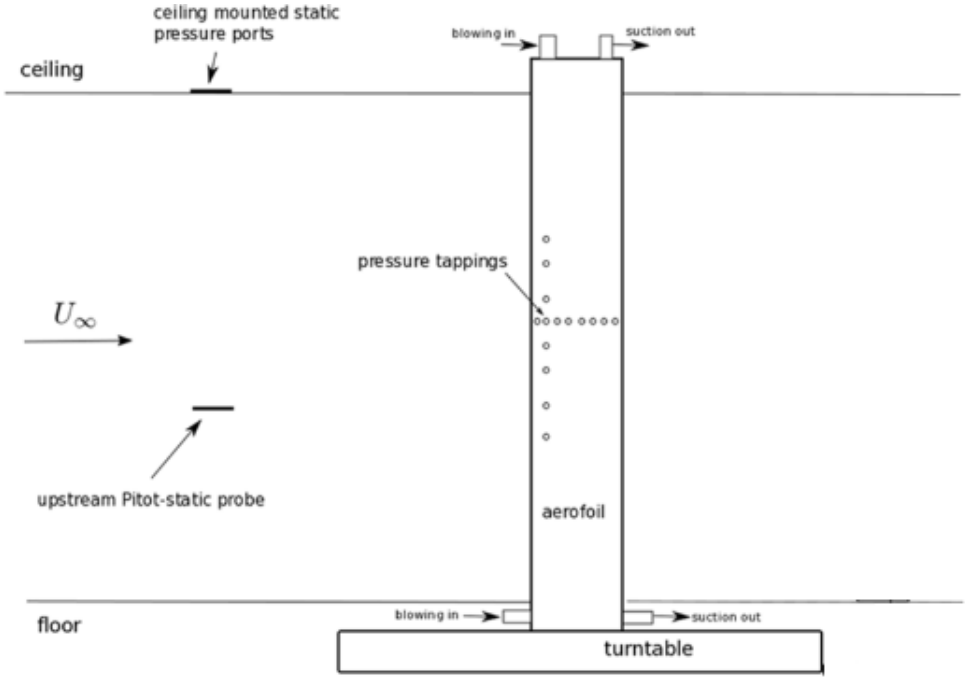

Fig. 5 Test arrangement side view

Fig. 6 SC-7500 fan connected to floor side circulation system

Mass flow measurement was taken using two mass flow meters. One meter was placed in the jet side of the loop for each of two circulation fans.

A. Model

A rigid wind tunnel model was supplied by SMAR Azure Ltd., along with the blowing and suction systems associated with the LE jet and TE suction. The model was aligned vertically in the tunnel, had a span and chord of 2.06 m and 0.24 m, respectively, a modified ellipse cross section and a uniform span-wise profile.

Two SC-7500 fans were used for circulation control. Due to the difficulties of scaling internal components down to the size of the wind tunnel model, circulation components were placed outside the tunnel with tubes transporting the air to and from the model.

The high-pressure line from the fans was fed into the top and bottom of the model by 60 mm plastic tubing, as shown in Fig. 6. This air was fed into a span length pipe contained within the model which had perforations along its length. This allowed the jet side airflow through into a plenum chamber before exiting the model through a small jet gap close to the leading edge.

Fig. 7 Model showing porous plate covered suction section

For the suction side, a second span length pipe was contained within the model and connected via plastic tubing to the suction side of the fans. Part of the circumference of this span length pipe was open to the airflow within the tunnel and

acted as a way of removing air near the trailing edge of the model. Along the span of the model, difference porosities of porous plate were used as a means of increasing flow resistance near the model ends and decreasing flow resistance near mid span, at the point furthest from the fans. The porous covering is shown in Fig. 7. This allowed for regulation of the suction velocities and ensured even suction mass flow along the span of the model. A ball valve was introduced into each of the two circulation lines as a means of controlling the resistance in the lines and altering the flow rates.

A lengthy preliminary set of configuration tests were conducted using varied distributions of porosity within the suction intake zone to equalise the intake conditions across the span of the model, and to calibrate estimates of jet velocity with associated flow rate in the pressurised line. Jet velocities were estimated from measurements of the dynamic pressure distribution at slot exit.

B. Procedure

The data recorded during the test program consisted of: reference static and stagnation pressures ahead of the model; stagnation pressure in the test chamber ahead of the model; model surface pressures; wind tunnel data for ambient air conditions and dynamic pressure; mass flow rates in the blowing and suction lines; and, jet injection air temperature.

The objective of the data analysis was to find model pressure lift and drag coefficients for different ratios of jet velocity to freestream velocity (circulation ratio). Lift per unit span at the model centre has been calculated from the standard integration of pressure data. Model surface pressure data was converted into pressure coefficient (upstream stagnation pressure and upstream static pressure used as reference pressures), and then integrated in the normal and chordwise directions. Lift and pressure drag coefficients were then obtained from these normal and tangential forces by axis transformation, with aerofoil chord used as the reference length.

Wind tunnel measurements need corrected for solid blockage, wake blockage and tunnel pressure gradient and turbulence. The increase in measured aerodynamic forces can be attributed to the presence of flow boundaries, or wake, increasing the flow velocity near the model, and can be considered as four separate effects: horizontal buoyancy, solid blockage, wake blockage and streamline curvature. For the current tests, standard tunnel corrections for solid blockage and streamline curvature were applied as described in [42].

Free stream air temperature varied between 273 K and 280 K across the tested conditions. Jet injection temperature was significantly higher due to heating by the fans and varied between 305 K and 315 K.

The AOA varied between 0° and 35°. The jet momentum coefficient C_μ was used as a measure of the momentum of the jet relative to the main flow. This was defined as:

$$C_\mu = \frac{\dot{m_j} V_j}{2 S \rho_\infty {V_\infty}^2} \quad (1)$$

where, $\dot{m_j}$ is the jet injection mass flow, V_j is the jet velocity, S is the reference area, ρ_∞ is the free stream air density and V_∞ is the free stream air velocity.

Over the full range of cases the jet momentum coefficient ranged between 0 and 0.7. After fixing the jet and suction mass flows for a set of cases, the jet momentum coefficient was varied by changing the wind tunnel free stream velocity.

A leading-edge trip strip was not used for the data recording as its inclusion was seen to not influence results. The Reynolds number across the tested conditions ranged from 80,000 to 240,000. Despite these values lying within laminar-turbulent transition region, the existence of a fast, turbulent jet near the leading edge is thought to have removed any influence of transition effects on results.

V. Numerical Setup

A. Solver Settings

The low speed, incompressible tests made use of a segregated approach in solving the flow equations for momentum and pressure. The physics continuum models are shown in Table I.

TABLE I
PHYSICS CONTINUUM SELECTION

Model type	Model Selected
Dimensions	2D
Time	Steady
Material	Gas
Flow	Segregated Flow
Equation of State	Constant Density
Viscous Regime	Turbulent

Grid Sequencing Initialization (GSI) was used to generate higher quality initial solutions by using an implicit, incomplete-Newton algorithm to approximate a first order, Euler flow field on levels of coarsened meshes [43]. Second-order upwind spatial discretization was used for the convection terms, and the second-order order central discretization for diffusion.

B. Governing Equations

For an incompressible fluid flow, the continuity and momentum equations are given as:

$$\frac{\partial u_i}{\partial x_i} = 0 \quad (2)$$

$$\rho u_j \frac{\partial u_j}{\partial x_j} = \frac{\partial \mathrm{p}}{\partial \mathrm{x_i}} + \frac{\partial}{\partial x_j}\left(\mu \frac{\partial u_i}{\partial x_j}\right) + \rho \frac{\partial(-\overline{u_i u_j})}{\partial x_j} \quad (3)$$

where u and v are velocity components in the x and y directions, p is the pressure and ρ and μ represent fluid density and viscosity [44].

For first order models, the turbulent momentum, heat and species flux have a direct relation with the mean flow. For these models, the Boussinesq hypothesis is used to define the unknown fluctuating term as a simple relationship with velocity gradients through the scalar and isotropic eddy viscosity, μ_T [45].

$$R_{ij} = -\rho\overline{u'_i u'_j} = 2\mu_T S_{ij} \quad (4)$$

$$S_{ij} = \frac{1}{2}\left(\frac{\partial u_i}{\partial x_j} + \frac{\partial u_j}{\partial x_i}\right) \quad (5)$$

where R_{ij} is the Reynolds stress tensor.

1. Spalart-Allmaras Turbulence Model

The Spalart-Allmaras (SA) turbulence model is a one-equation model which determines the turbulent eddy viscosity by solving a transport equation for the modified diffusivity in order to determine the turbulent eddy viscosity [46]. This model was applied in its standard, low Reynolds formulation using a y+ value no greater than 1 over all wall surfaces.

The empirical curvature correction approach of Spalart and Shur (SARC) has been applied to more accurately capture with the large streamline curvature due to jet attachment [47].

2. K-Omega-SST

A well-documented shortcoming of standard eddy viscosity models is poor prediction for flows exhibiting anisotropic turbulence such as with strong streamline curvature or stress driven secondary flows [46]. As a means of investigating the influence of these effects for the studied geometry, comparisons are made with a more advanced model – k-omega-SST.

As a modification to the Standard K-omega Model, Menter proposed the shear stress transport model (SST) which acts to use a blending function to favour a K-epsilon type model near the farfield boundaries and a K-omega model near the walls [48]. One further modification to this model is again the inclusion of curvature correction parameters which alter the turbulent kinetic energy production term according to the local effects of rotation and vorticity [46]. This modification is commonly known as SST-CC.

3. Darcy–Forchheimer Law

The perforated plate that covers the aerofoil TE suction section was simulated using the porous region model within Star-CCM+. For 2D simulation, this has the effect of constraining the flow within the porous region to normal to the outer surface.

The pressure drop across this region is defined by the Darcy–Forchheimer law as [46],

$$\frac{\Delta P}{l} = -(P_i|v| + P_v) \quad (6)$$

where, ΔP is the pressure drop, l is the porous region thickness, v is the superficial velocity and P_i and P_v are the inertial and viscous resistance components. For the flows being studied, the inertial resistance component has a far greater influence on the pressure drop relative to the viscous coefficient. The Darcy–Forchheimer law was set equal to Idelchik's empirical relationship for the resistance coefficient of perforated plates at 40% porosity [49]. This resulted in a value of 312.5 $\mathrm{kg/m^4}$ being selected for the inertial resistance coefficient.

C. Meshing

Meshing was controlled by the Star-CCM+ 2D automatic mesher using the polygonal cell and prism layer models - the latter used to capture the boundary layer region adjacent to the surface. Prism layers extend well into the domain as a method of accurately capturing the interaction and entrainment of the high momentum jet with surrounding air. The $y+$ values are less than 1 on wall boundaries for all cases. The cell count was approximately 300,000 with a grid convergence study showing an increase to 400,000 cells was only met with a lift coefficient and pressure drop change of 0.8% and 1.1%, respectively, for a nominal case. The model geometry associated with the jet inlet is recessed to allow space for the jet flow to develop and then to fully capture the turbulent mixing and energy transfer between the jet and main flow.

D. Boundary Conditions

The pressure boundaries across the LE injection and TE suction surfaces were iterated so that the mass flows matched those recorded from experiment. The selection of the TE boundary condition was met with significant results sensitivity. When considering more conventional co-flow jet type aerofoils, omitting the porous region and using a suction slot gap which extracts air tangentially to the aerofoil surface rather than at right angles, these instabilities and issues were not met. The proximity of the enforced surface boundary condition to both the porous region and significant flow features may have contributed to the sensitivities in the SWAP simulations. Although the exact cause was unclear, the iterated pressure boundary condition was found to most accurately simulate results. The influence of wind tunnel walls was included within the simulation. The jet flow direction is normal to the boundary.

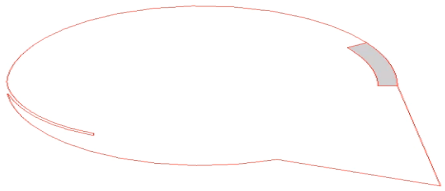

Fig. 8 SWAP geometry (not to scale)

A velocity inlet boundary was used for the inlet and had a turbulence intensity of 1% with a length scale of 0.05 m, representing the wind tunnel upstream grid spacing. A pressure outlet boundary was used for the downstream tunnel face.

Fig 8 shows the approximate locations of the LE jet surface, TE suction surface and porous region (highlighted grey). Due to IPR constraints, this figure is not to scale.

E. Convergence Criteria

Asymptotic solution monitors were placed on the lift coefficient, drag coefficient, pressure drop, jet inlet mass flow and suction outlet mass flow. These convergence criteria were satisfied when the normalised change in these values fell below 5×10^{-5} over 20 iterations. The pressure drop was

defined as the change in total pressure between the recessed jet inlet boundary and the suction outlet boundary. Additional monitors were placed on the residuals for relevant flow variables.

VI. Results and Discussion

A. Experimental Results

Selected results are presented which highlight significant features of the data from the various test cases. All load coefficients are generated from measured loads through non-dimensioning by the freestream dynamic pressure and aerofoil chord.

Fig. 9 shows the variation in normalised lift coefficient against AOA as the circulation percentage, Q, increases. This circulation percentage increases with the jet momentum coefficient. The data represents a fixed mass flow for LE injection and TE suction. Circulation percentage is varied by changing the free stream velocity.

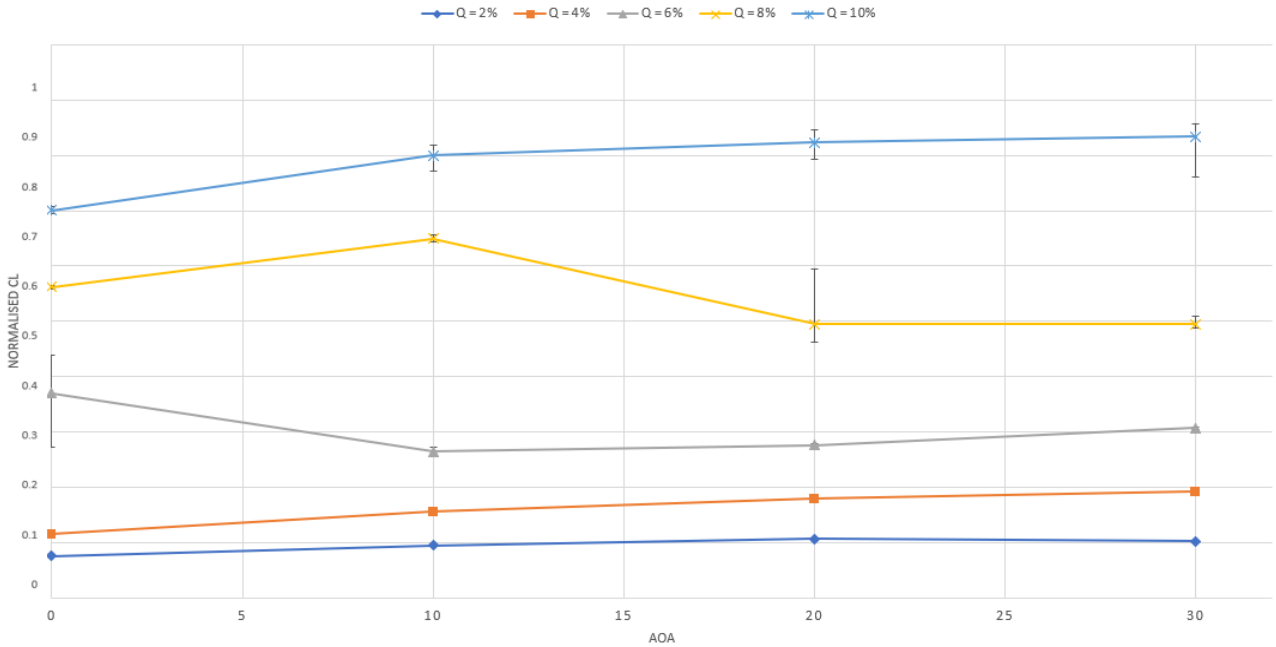

Fig. 9 Normalised lift coefficient vs. AOA for various circulation percentage

The data generally follow a consistent trend, with increased lift coefficient with circulation ratio across the range of angles of attack investigated. The characteristic curves are relatively flat with the lift magnitudes seeming to flip between two states at a critical value of C_μ. The flow field for cases near these critical C_μ values did not exhibit monotonic behaviour. Intermittent, unsteady separation from a point just ahead of the air intake region was indicated during a number of test cases by the behaviour of tufts on the aerofoil surface. These critical circulation points dictated a transition between fully attached flow and partially separated flow.

Having completed five, two second data samples for each combination of mass flow, momentum coefficient and AOA, it was thought that giving a pure average for the pressure lift and drag for each case would lose some data fidelity and remove information about cases which exhibit this detachment and reattachment of flow. Error bars have been introduced, not as a measure of the experimental error, but to illustrate the unsteadiness in the lift and drag results. The data point passes the 5-sample average and the limits of each points error bar represent the highest and lowest C_l and C_d values for each case. Points with large error bars represent cases which exhibit this unsteadiness and are in transition between purely attached or detached flow.

Reference to Fig. 9 shows the clear detachment point of the 8% circulation percentage case at 20 degrees AOA. This point exhibits the high error bars that are indicative of detaching and reattaching flow and, beyond this point, lift coefficient is dramatically reduced although retaining its flat shape. As would be expected, increased circulation percentage, and therefore higher momentum fluid being injected into the inner part of the shear layer, results in these detachment points happening at a larger AOA.

Fig. 10 shows a typical variation of lift coefficient with jet momentum coefficient over a range of incidence angles. The trend lines exhibit a characteristic `leap frogging', whereby the data relating to the lower angles of attack jumps from lowest C_l to highest C_l due to the flow attaching earlier along the incidence sweep for lower C_μ values. Taking the 0-degree (blue diamond) case as an example, the C_l attaches at a C_μ value between 0.16 and 0.23 which corresponds to a dramatic C_l increase. This type of jump is repeated for the higher AOA cases, albeit at higher blowing momentum coefficient values.

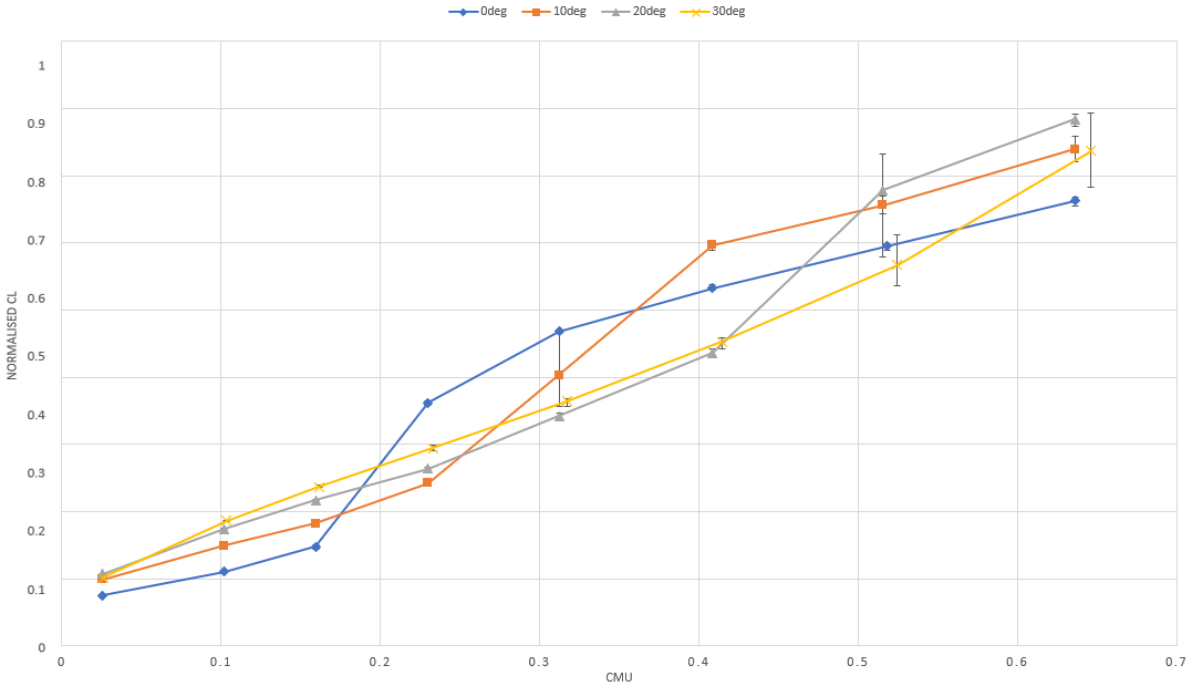

Fig. 10 Normalised lift coefficient vs. C_μ for various AOA

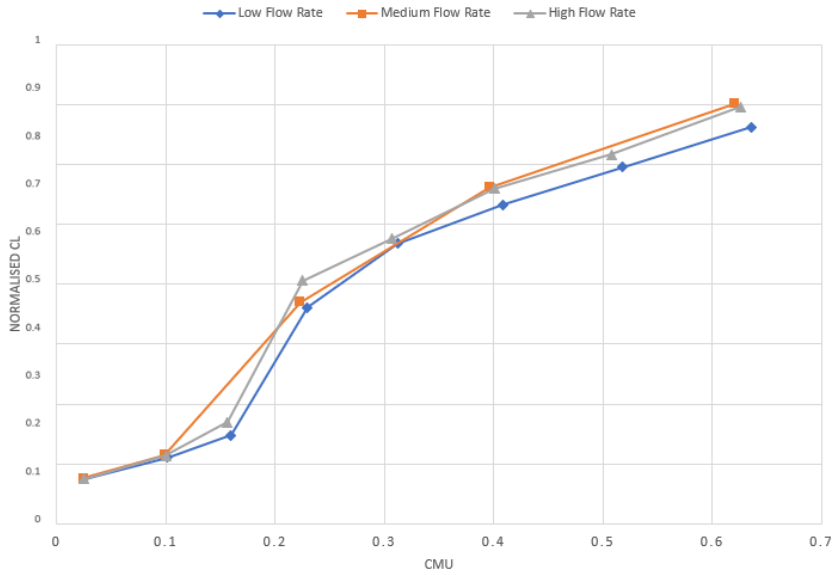

Fig. 11 Normalised lift coefficient vs. C_μ for changing circulation percentage at 0° AOA

Figs. 11 and 12 give results for the lift coefficient variation with jet momentum coefficient for three different flow rates at fixed incidence angles. The lift trend lines relating to the three different flow rates are relatively collected, showing that there does not seem to be too much variation of lift coefficient for different jet flow rates if the C_μ values are consistent.

In regard to the critical C_μ value which causes flow to attach, this again seems relatively consistent between different flow rates. Reference to Fig. 11, the 0-degree AOA, C_l vs. C_μ graph, shows a consistent jump in lift coefficient as blowing momentum coefficient increases between 0.16 and 0.23 for all three flow rates tested.

B. Numerical Results

Selected cases have been simulated using the Spalart-Allmaras model with rotation correction (SARC) and the K-omega-SST model with curvature correction (SST-CC). The CFD results have been compared with experiment in the form of normalised surface pressures. A common feature of the

numerical data was variable prediction performance of the turbulence models depending on the blowing momentum coefficient, C_μ.

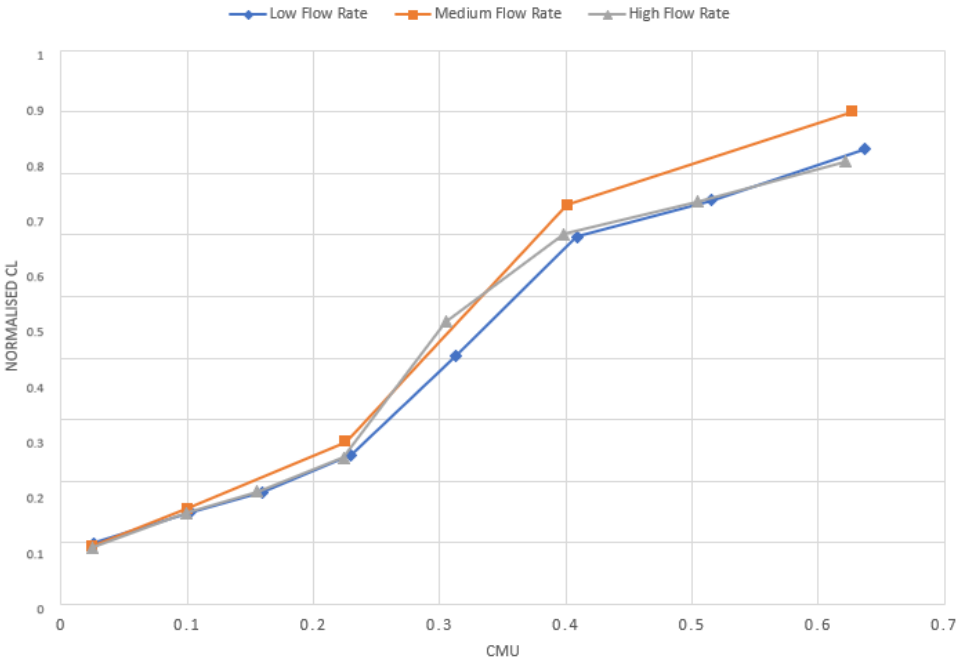

Fig. 12 Normalised lift coefficient vs. C_μ for changing circulation percentage at 10° AOA

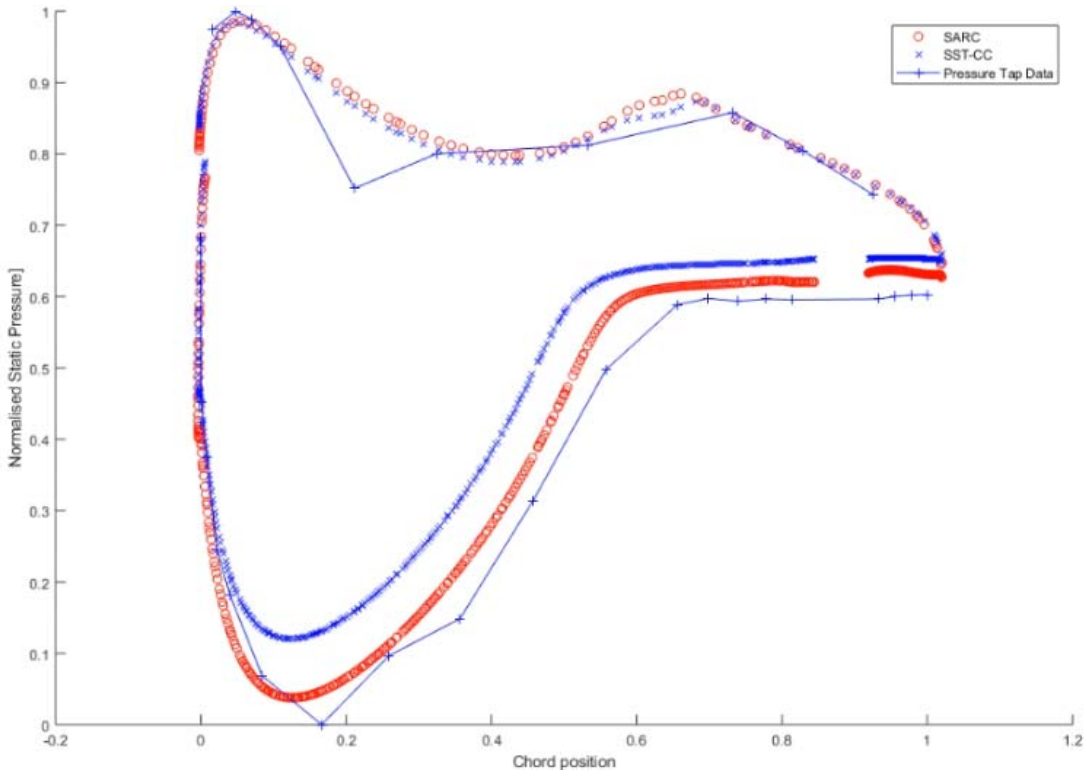

Fig. 13 Normalised surface static pressure comparison; AOA = 15 deg, C_μ = 0.03

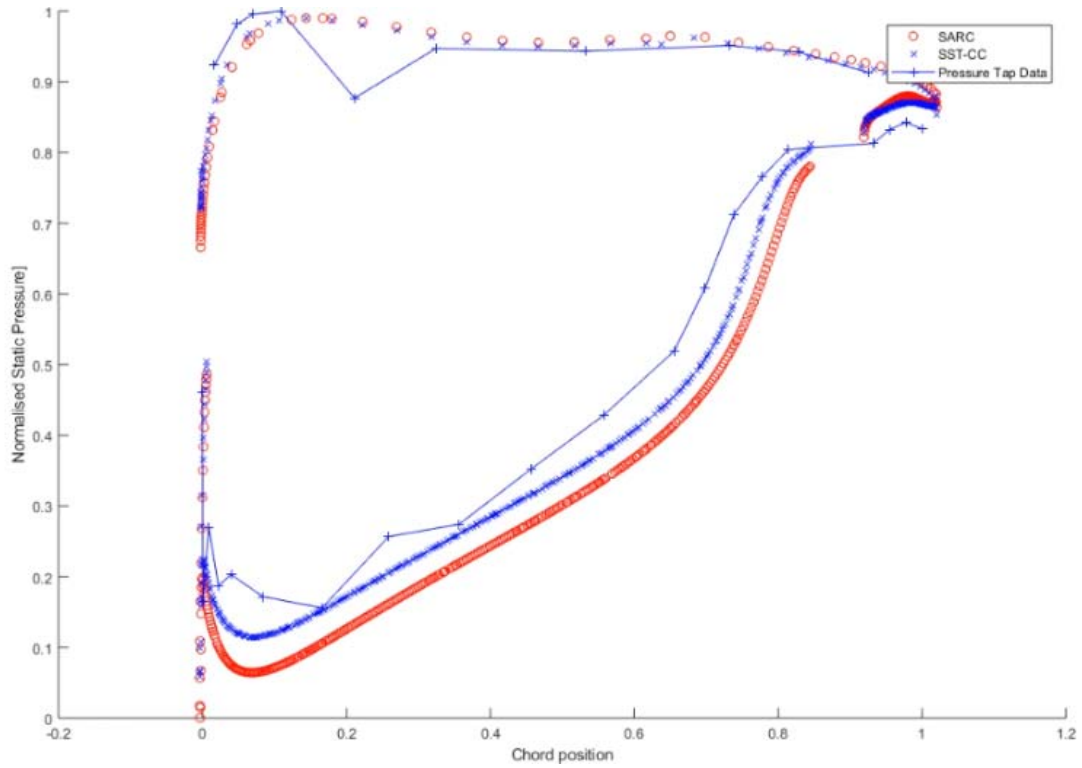

Fig 14 Normalised surface static pressure comparison. Aoa = 15 deg, C_μ = 0.23

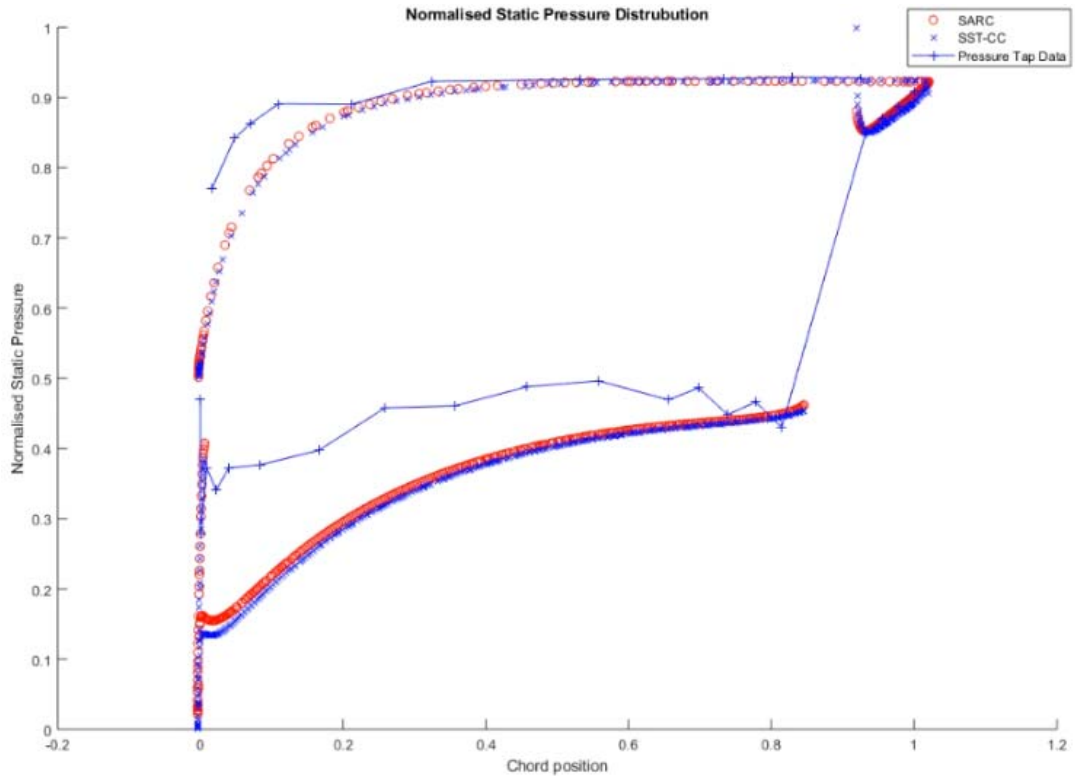

Fig. 15 Normalised surface static pressure comparison. Aoa = 15 deg, C_μ = 0.5

The SARC model performed very well for low blowing coefficients; however, as the blowing coefficient increased

and the system moved towards the critical attachment points identified during the experimental tests, the SARC model began to slightly overpredict surface pressures relative to both experiment and the SST-CC model. After passing the critical attachment point, both turbulence models were met with a sharp drop off in accuracy and significantly overpredicted the aerofoil suction pressure for fully attached flow cases. Figs. 13-15 illustrate this effect for a nominal flow rate case. Firstly, Fig. 13 shows the comparison of the two turbulence models with experimental data for 15° AOA for a low blowing momentum coefficient value of 0.03.

Finally, Fig. 15 illustrates the surface static pressure comparison for a larger jet momentum coefficient value of 0.5.

While both turbulence models show good agreement with each other for this case, both have significantly overpredicted lift, with the discrepancy relative to experimental data appearing to increase towards the upstream aerofoil surfaces.

The data were typical of the numerical routine - giving very good surface pressure distribution for detached flow cases and then over predicting the lift when the flow is fully attached.

Several possibilities were considered to account for this discrepancy between CFD and experiment. It was proposed that the large discrepancy at high $C\mu$ may be primarily due to the inadequacy of a RANS turbulence model to simulate the unsteady jet-mixing or vortex shedding processes. Despite some cases clearly exhibiting separated flow, steady state results are presented for the CFD cases. Unsteady solutions showed minimal change for the vast majority of cases and were met with a dramatically increased computational cost. This feature of RANS circulation control modelling has been previously noted by Swanson et al. who, although highlighted that the "vortex pair usually occurring behind the blunt trailing edge is conspicuously absent", found good lift agreement with experimental results when using steady state RANS methods [37]. Wang et al. also found good agreement between steady state RANS solutions and separated flow experimental data for circulation control applications [50].

Although circulation control aerofoils commonly have thick profiles relative to conventional aerofoils, most of the literature showing good agreement with RANS models examines a far thinner section than is considered here. This iteration of the SWAP device has a thickness greater than 50% chord, a further reason why the geometry presents difficulties when numerically solving the flow field.

A well-documented shortcoming of standard eddy viscosity models is poor prediction for flows exhibiting anisotropic turbulence such as with strong streamline curvature or stress driven secondary flows. These are chief features of circulation control flows and, therefore, a limited set of Reynolds Stress Model (RSM) simulations were performed as a means of observing the effect of a more advanced turbulence model on the surface static pressure. The Reynolds stress model provides differential transport equations which allow evaluation of turbulence stress components. Again, this model failed to offer an improved correlation with experimental data, confirming the results of Wilde [51] who has also previously found limited performance improvements between RSM and SST-CC flows for circulation control applications. The simulations were also met with far greater cost and computational instability. A more advanced turbulence consideration, such as Detached Eddy Simulation (DES), is computationally unfeasible given this work's future goal of performing a parametric optimisation study.

Mass flow measurements were solely used for confirming that the circulation momentum coefficient was set as intended. With no dependable method of measuring the jet and suction total pressures, there was no way to ensure that the corresponding boundary conditions replicated real world conditions. Future experimental tests will look into methods of recording jet injection and suction chamber pressures as a second means of validating the numerical setup of the circulation system.

Unsteady variations in jet and suction velocities along the model span may also influence the results. During configuration of the circulation system it was known that there were slight jet velocity variations along the model span. A means of confirming if these variations were proportional to jet injection coefficient was not established.

The maximum power of the circulation fans acted as a limiting factor for the range of jet momentum coefficient values and therefore limited the wind tunnel velocity. This has meant that the range of Reynolds number investigated during the experimental tests is between 80,000 and 240,000. These numbers lie mainly around or below the transition region of an elliptical type section and, although the use of a tripping strip showed little influence on results, there may be other, less clear factors that are influencing results in a regime which is notoriously difficult for RANS based models to predict.

VII. Conclusion

Wind tunnel tests have been carried out at the University of Glasgow NWTF (deHavilland wind tunnel) on a 1:20 scale model of a SWAP. The tests were aimed at obtaining surface pressure data for an alternative ship propulsion device. This device will be retrofitted to existing vessels and aims to reduce their reliance on fossil fuel-based propulsion systems by using clean energy from the wind.

The experiments consisted of calibrating the circulation system, followed by a series of tests to record surface pressures at the mid-span of the model. A large parameter space was investigated, covering a range of circulation ratios, angles of attack and circulation flowrates. The data demonstrates that significant performance advantages can be gained in applying a co-flow jet type circulation concept to thick, modified ellipse aerofoil sections. Increasing injection momentum coefficient was met with an increase in lift coefficient for all cases.

One significant feature of the tests was the identification of critical combinations of injection momentum coefficient and AOA. These combinations represent tipping point flow conditions, with flow detachment and reattachment happening at a transition point between two distinct flow states.

Numerical simulations have been carried out and validated against the experimental data. Good agreement was found

when comparing simulation and experiment for low jet momentum coefficient, detached flow cases. The SARC model outperformed the SST-CC model for very low jet momentum coefficient values and flows exhibiting the highest degree of separation. Both turbulence models showed poor agreement for fully attached flow cases and overpredicted peak surface suction pressures. The results appear to indicate that steady state RANS turbulence models have difficulty in accurately predicting surface pressures for very thick, circulation control aerofoils over a wide range of flow conditions. Evaluation of the numerical setup is partially clouded by high results sensitivity to the definition of the suction face boundary condition and its interaction with a porous-region type implementation of a perforated plate.

Further work is required in confirming the SWAP device as an effective commercial proposition. This project will continue by considering a parametric optimisation study and further wind tunnel testing and validation.

REFERENCES

[1] United Nations. (2018). Oceans and the Law of the Sea. Available: http://www.un.org/en/sections/issues-depth/oceans-and-law-sea/index.html. Last accessed 20th Jul 2018. W.-K. Chen, Linear Networks and Systems. Belmont, CA: Wadsworth, 1993, pp. 123–135.

[2] Organization, I.M. Sulphur 2020 – Cutting Sulphur Oxide Emissions. 2018 (cited 2018 6th June); Available from: http://www.imo.org/en/MediaCentre/HotTopics/Pages/Sulphur-2020.aspx.

[3] Organization, I.M. UN body adopts climate change strategy for shipping. 2018 (cited 2018 5th June); Available from: http://www.imo.org/en/MediaCentre/PressBriefings/Pages/06GHGinitialstrategy.aspx

[4] Register, L.s., Low carbon pathways 2050, I. Sustainability, Editor. 2016: Online

[5] Shukla, P. C., Ghosh, K. (2009). Revival of the Modern Wing Sails for the Propulsion of Commercial Ships. World Academy of Science, Engineering and Technology International Journal of Physical and Mathematical Sciences. 3 (3)

[6] Smith, T. et al. (2013). Analysis techniques for evaluating the fuel savings associated with wind assistance. Low Carbon Shipping Conference.

[7] Carter, R., Boat remains and maritime trade in the Persian Gulf during the sixth and fifth millennia BC. Antiquity, 2006. 80(307): p. 52-63.

[8] Carter, W. E., & Carter, M. S. (2010). The Age of Sail: A Time when the Fortunes of Nations and Lives of Seamen Literally Turned with the Winds Their Ships Encountered at Sea. Journal of Navigation, 63(04), 717–731. doi:10.1017/s0373463310000263

[9] Michael Lang, The Journal of Modern History, Vol. 78, No. 4 (December 2006), pp. 899-931, Published by: The University of Chicago Press, DOI: 10.1086/511251, https://www.jstor.org/stable/10.1086/511251

[10] Chrzanowski, I. (1980). Shipping in the 1980s—a future with uncertainty? Maritime Policy & Management, 7(1), 1–8. doi:10.1080/03088838000000048

[11] Viola, I. M., Sacher, M., Xu, J., & Wang, F. (2015). A numerical method for the design of ships with wind-assisted propulsion. Ocean Engineering, 105, 33–42. doi: 10.1016/j.oceaneng.2015.06.009

[12] Copuroglu, H. I., & Pesman, E. (2018). Analysis of Flettner Rotor ships in beam waves. Ocean Engineering, 150, 352–362. doi:10.1016 /j. oceaneng.2018.01.004

[13] Searcy, T. (2017). Harnessing the wind: A case study of applying Flettner rotor technology to achieve fuel and cost savings for Fiji's domestic shipping industry. Marine Policy, 86, 164–172. doi:10.1016/j.marpol.2017.09.020

[14] Takayama, S., & Aoki, K. (2005). Flow characteristics around a rotating grooved circular cylinder with grooved of different depths. Journal of Visualization, 8(4), 295–303. doi:10.1007/bf03181548

[15] THOM, A. 1926 The pressure round a cylinder rotating in an air current. ARC R. & M. 1082

[16] Prandtl, L. (1925). Application of the "Magnus Effect" to the Wind Propulsion of Ships. Die Naturwissenschaft. 13, p93-108.

[17] Craft, T., Johnson, N., & Launder, B. (2013). Back to the Future? A Re-examination of the Aerodynamics of Flettner-Thom Rotors for Maritime Propulsion. Flow, Turbulence and Combustion, 92(1-2), 413–427. doi:10.1007/s10494-013-9486-4

[18] Suominen, T, 2015, Rotor pilot project on M/S Estraden of Bore fleet, Bachelor of Marine Technology, Satakunta University of Applied Sciences

[19] Airbus. (2018). High-flying Airbus technology comes down to Earth for use on ships. Available: https://www.airbus.com/newsroom/news/en/2018/09/high-flying-airbus-technology-comes-down-to-earth-for-use-on-shi.html. Last accessed 12th Sep 2018

[20] Kiteboat. (2018). Kiteboat Project. Available: https://project.kiteboat.com/design/. Last accessed 12th Sep 2018

[21] Kukner et al. (2016). Renewable Energy Options and an Assessment of Wind-Based Propulsion Systems for Small Crafts. Naval Academy Scientific Bulletin. 19

[22] Naaijen, Peter, and Vincent Koster. "Performance of auxiliary wind propulsion for merchant ships using a kite." 2nd International Conference on Marine Research and Transportation. 2007

[23] Traut, M., Gilbert, P., Walsh, C., Bows, A., Filippone, A., Stansby, P., & Wood, R. (2014). Propulsive power contribution of a kite and a Flettner rotor on selected shipping routes. Applied Energy, 113, 362–372. doi:10.1016/j.apenergy.2013.07.026

[24] Yoshimura, Yasuo. (2002). A Prospect of Sail-Assisted Fishing Boats. Fisheries Science. 2, p1815-1818

[25] Charrier, B., Constans, J., Cousteau, J.-Y., Daïf, A., Malavard, L., & Quinio, J.-L. (1985). Fondation Cousteau and windship propulsion 1980 – 1985 system Cousteau - Pechiney. Journal of Wind Engineering and Industrial Aerodynamics, 20(1-3), 39–60. doi:10.1016/0167-6105(85)90011-x

[26] Hcini, C., Abidi, E., Kamoun, B., & Afungchui, D. (2016). Numerical prediction for the aerodynamic performance of Turbosail type wind turbine using a vortex model. Energy, 109, 287–293. doi:10.1016/j.energy.2016.04.113

[27] Guerri, O.; Liberge, E.; Hamdouni, A. (2016). Numerical Simulation of the Turbulent Flow around an Oval-Sail. Journal of Applied Fluid Mechanics. 9 (4), p2009-2023

[28] Konstantinos, K. et al (2018). Foundations of Circulation Control Based Small-Scale Unmanned Aircraft: A Comprehensive Methodology from Concept to Design and Experimental Testing: Springer International Publishing

[29] Imants Reba. (1966). Applications of the Coanda Effect. Scientific American. 214, pp. 84-93.

[30] Rodman, L.C., Wood, N.J. and Roberts, L., 1989. Experimental investigation of straight and curved annular wall jets. *AIAA journal*, *27*(8), pp.1059-1067.

[31] Newman, B.G., 1961. The deflection of plane jets by adjacent boundaries-Coanda effect. *Boundary layer and flow control*.

[32] Allery, C., Guerin, S., Hamdouni, A., & Sakout, A. (2004). Experimental and numerical POD study of the Coanda effect used to reduce self-sustained tones. Mechanics Research Communications, 31(1), 105–120. doi: 10.1016/j.mechrescom.2003.08.003

[33] Abdul Hamid, M. F. (2011). Numerical Simulation and Analysis of Coanda Effect Circulation Control for Wind Turbine Application Considerations IIUM Engineering Journal, 12(3). Retrieved from http://journals.iium.edu.my/ejournal/index.php/iiumej/article/view/68

[34] Storm, T., & Marshall, D. (2010). Assessing the v2-f Turbulence Models for Circulation Control Applications. 48th AIAA Aerospace Sciences Meeting Including the New Horizons Forum and Aerospace Exposition. doi:10.2514/6.2010-1054

[35] Rumsey, C., & Nishino, T. (2011). Numerical Study Comparing RANS and LES Approaches on a Circulation Control Airfoil. 49th AIAA Aerospace Sciences Meeting Including the New Horizons Forum and Aerospace Exposition. doi:10.2514/6.2011-1179

[36] Swanson, R., Rumsey, C., & Anders, S. (2005). Progress Towards Computational Method for Circulation Control Airfoils. 43rd AIAA Aerospace Sciences Meeting and Exhibit. doi:10.2514/6.2005-89

[37] Swanson, R.C., Rumsey, C.L. and Anders, S.G., 2006. Aspects of numerical simulation of circulation control airfoils. Progress in astronautics and aeronautics, 214, p.469

[38] Zha, G.-C., and Paxton, D. C., "A Novel Flow Control Method for Airfoil Performance Enhancement Using Co-Flow Jet," Applications of Circulation Control Technologies, edited by Joslin, R. D. and Jones,

G.S., Progress in Astronautics and Aeronautics, Vol. 214, AIAA, Reston, VA, 2006, pp. 293–314, Chap. 10

[39] Zha, G., Gao, W., & Paxton, C. D. (2007). Jet Effects on Coflow Jet Airfoil Performance. AIAA Journal, 45(6), 1222–1231. doi:10.2514/1.23995

[40] Xu, H., Xing, S. and Ye, Z., 2015. Numerical simulation of the effect of a co-flow jet on the wind turbine airfoil aerodynamic characteristics. *Procedia Engineering*, *126*, pp.706-710.

[41] Skinner, S.N. and Zare-Behtash, H., 2017. Semi-span wind tunnel testing without conventional peniche. *Experiments in Fluids*, *58*(12), p.163.

[42] Barlow, J.B., Rae Jr, W.H. and Pope, A., 2015. Low speed wind tunnel testing. *INCAS Bulletin*, *7*(1), p.133.

[43] Shankara, P. and Snyder, D., 2012, June. Numerical simulation of high lift trap wing using STAR-CCM+. In *30th AIAA Applied Aerodynamics Conference* (p. 2920).

[44] Gualtieri, C., Jiménez, P.L. and Rodríguez, J.M., 2009, August. A comparison among turbulence modelling approaches in the simulation of a square dead zone. In *Proceedings of the 19th Canadian Hydrotechnical Conference, Vancouver, BC, Canada* (pp. 9-14).

[45] Yoon, G.H., 2016. Topology optimization for turbulent flow with Spalart–Allmaras model. *Computer Methods in Applied Mechanics and Engineering*, *303*, pp.288-311.

[46] Siemens (2018). *STAR-CCM+ Documentation Version 13.02*: Siemens PLM Software

[47] Shur, M., Strelets, M., Travin, A. and Spalart, P., 1997. Turbulence modeling in rotating and curved channels-assessment of the Spalart-Shur correction term. In *36th AIAA Aerospace Sciences Meeting and Exhibit* (p. 325).

[48] Asnaghi, A., Svennberg, U. and Bensow, R.E., 2019. Evaluation of curvature correction methods for tip vortex prediction in SST k− ω turbulence model framework. *International Journal of Heat and Fluid Flow*, *75*, pp.135-152.

[49] Idelchik, I.E., 2017. *Flow resistance: a design guide for engineers*. Routledge.

[50] Wang, B., Haddoukessouni, B., Levy, J. and Zha, G.C., 2008. Numerical investigations of injection-slot-size effect on the performance of coflow jet airfoils. *Journal of Aircraft*, *45*(6), pp.2084-2091.

[51] Wilde, D., 2010. Analysis of Curvature Effects on Boundary Layer Separation and Turbulence Model Accuracy for Circulation Control Applications.